CMES, vol.4, no.3&4, pp.473-488, 2003

Entry Length and Wall Shear Stress in Uniformly Collapsed-Pipe Flow

M. Thiriet[1], **S. Naili**[2] **and C. Ribreau**[2]

Abstract: The laminar steady flow of incompressible Newtonian fluid is studied in rigid pipes with cross configuration of a collapsed tube to determine both the entry length and the wall shear stress (WSS). The cross section shapes have been defined from the collapse of an infinitely long elastic tube subjected to an uniform transmural pressure. Five characteristic collapsed configurations, from the unstressed down to the point-contact states, with a finite and infinite curvature radius at the contact point, are investigated, although the wall contact is not necessary observed in veins. Such collapsed shapes induce cross gradient in WSS in straight pipes. The Navier-Stokes equations, associated with the classical boundary conditions, are solved using a finite element method. The numerical tests are performed with the same value of the volume flow rate whatever the tube configuration. Entry length, axial and cross variations in WSS are computed to design flow chambers in order to explore the mechanotransduction function of the endothelial cells.

keyword: collapsed tube flow, contact, entry length, finite element method, flow chamber design, wall shear stress.

1 Introduction

Biofluids (air, blood, lymph, urine, ...) are conveyed in flexible vessels which undergo deformation under varying transmural pressures $p = p_i - p_e$ (p_i, p_e: internal and external pressures). In the present work, the biofluid of interest is the blood. The blood is a suspension of cells and particles. In large blood vessels, the ratio between the vessel length scale and the convected particle characteristic size is such that the blood is considered as a continuous homogeneous medium. The computational model is then based on Navier-Stokes equations. The red blood cells (RBC) play a major role on the rheological behaviour of the blood due to both their size and number; the blood is thus supposed to behave like a concentrated suspension of RBCs. In steady state conditions, the blood has a shear-thinning behaviour (Chien, 1970). The sigmoid relationship between the shear rate $\dot{\gamma}$ and the fluid viscosity μ is explained by RBC agregation at low shear rates associated with high viscosity values (maximum: μ_0) in the one hand while RBC deformation and orientation lead to a low viscosity plateau μ_∞ at high shear rates $\dot{\gamma} \geq \sim 10^2\, s^{-1}$ (Newtonian behaviour). When both RBC agregation and deformation are inhibited, μ_0 is close to μ_∞ (Chien, 1975). In the present study, RBCs are assumed neither to agregate due to the undergone shear history nor to deform in large vessels; consequently, the blood is supposed to be Newtonian.

The blood macrocirculation, *i.e.* the part of the circulation composed of blood vessels of $d_h > 300\,\mu m$, is made of two vessel types whether the vessel conveys the blood from the cardiac pump to the organs or to the heart from the periphery: (i) proximal (from the heart) elastic and distal muscular arteries and (ii) superficial and deep veins respectively. Arteries dilate while the pressure waves are travelling through the vascular bed. The storage of blood by the aorta, which is an elastic artery, during the systolic ejection of blood by the left ventricule transforms the transient blood flow at the heart exit (protosystolic starting - protodiastolic stopping flow) into a pulsatile flow in the arterial tree, with more or less back flow during the diastole (blood flows then permanently through the distal arteries during the cardiac cycle). This compliant property of the proximal arteries is the so-called Windkessel effect. The cross-sectional area A of the artery, which is circular, is inflating whereas p, which is positive, is increasing. The cross-sectional shape may be sligthly affected because of the non-uniform distribution of p over the entire vessel perimeter. Veins constitute the storage compartment of the blood vessel network (the vein compliance allows the blood volume to reside mainly - up to

---

[1] LJL2, UMR CNRS 7598, UPMC, F-75252 Paris and INRIA, Projet BMG, BP 105, F-78153 Le Chesnay.
[2] LMP/B2OA, UMR CNRS 7052, UPVM, F-94010 Créteil.

70 % - in the venous collector). However, veins can be subjected to negative transmural pressures. The superficial veins are much more deformable than the deep ones (Bassez *et al.*, 2001); they may experience changes both in cross-sectional area and shape when they are subjected to negative transmural pressures during natural prompting, functional testing maneuvers or therapeutic actions, even if p is uniformly distributed in the entire cross section (*e.g.* Ribreau and Thiriet, 1998, Thiriet *et al.*, 2001).

The large and medium sized veins, located far from the trunk, are assumed to be free from the periodic variations of the thoracic or abdominal pressures induced by the respiration and the periodic outlet effects of the cardiac pump. Furthermore, at rest, the respiratory motions have small amplitude and the venous flow is not affected by alternate muscle contractions and relaxations. The Windkessel effect is supposed to damp the small unsteady factors from the downstream segments of the venous bed. The flow at rest in the large veins of the inferior limbs, for instance, can be assumed to be steady.

The wall of the blood vessels is circumferentially composed of three layers, the internal thin intima, the muscular media and the external adventitia. The endothelial cells (EC) constitute the interface between the flowing blood and the solid vessel wall. ECs are involved in coagulation, hemostasis, immune pathways, vessel wall growth and remodelling. Moreover, they locally control the vasomotor tone of the media by producing both contracting and relaxing agents, and thus the lumen size available for the blood convection. The synthesis of vasoactive factors is triggered by the stresses imposed on the cell wetted surface by the circulating blood (local flow-induced regulation of the blood circulation). Since two decades, a huge set of investigations has been performed to explore either the cell rheology or the behaviour of mechanical stress-subjected cells. Several rheological techniques have been developed: micropipette technique, twisting magnetocytometry (*e.g.* Laurent *et al.*, 2000) and optical twizer (*e.g.* Lenormand *et al.*, 2000). Flow chambers coated with homogeneous confluent monolayer of EC cultures are used for EC exposure to laminar shear stresses (*e.g.* Franke *et al.*, 1984, Olesen *et al.*, 1988, DePaola *et al.*, 1992, Barbee *et al.*, 1994, Sun *et al.*, 2000).

The magnitude and orientation of the wall shear stresses (WSS) depend both on the axial - and transverse tube configuration and on the flow pattern. Change in direction of the WSS axial component occurs when the pulsatile flow generates a back flow in the whole vessel lumen or in a layer near the wall. A WSS circumferential component appears when the vessel presents a curvature of its axis. Cross variation in wall curvature, which are also observed in collapsed tubes due to the transverse bending of the wall, induces transverse gradient of the WSS axial component. The WSS cross changes in a fully-developed steady laminar flow has been investigated in two-dimensional collapsed configuration by Naili and Ribreau (1999). Using their results, a peculiar flow chamber has been designed to expose ECs to biaxial stress (Haond *et al.*, 1999). The axially uniform cross-section of the test section, located downstream from a long pipe to ensure a fully-developed flow, has the shape of a line-contact cross-section of a thin-walled collapsible tube in a bilobal collapse mode. The cross-section configuration used by these authors was not aimed at mimicing actual collapsed veins but creates at the cell scale a shear stress which generates two forces applied at the cell inertia center: (i) a shear force which stretches the cell in the streamwize direction, *e.g.* the force arising from the shear stress at the cell inertia center, and (ii) a shear torque which twists the cell perpendicularly to the cell plane, induced by the WSS transverse gradient. Four regions of the wetted cell culture were defined by these investigators: (i) region I near the contact point where both the WSS and its transverse gradient (WSSTG) are small, (ii) region II of low velocity flow where WSS is low but WSSTG is significant, (iii) region III with a change in wall curvature sign where both the WSS and WSSTG are great and (iv) region IV where WSS reaches its highest values but WSSTG is small. In region II, these authors discussed the role of the torsion in the EC detachment both from the wall of the flow chamber and from the cell layer, *i.e.* from the adjoining ECs. The present work is aimed at providing some design parameters for flow chambers as well as understanding tools for EC rheology and EC biological functions.

2 Method

The numerical simulations of developing steady laminar flows of an incompressible homogeneous Newtonian fluid are carried out for three Reynolds numbers (35, 500, 1000). Each investigated rigid smooth straight conduits have axially uniform cross section which represent the cross shape in unstressed and balanced states corresponding to collapsed configurations at selected values of the transmural pressure. The explored vessel are straight of axis $\hat{\mathbf{e}}_z$.

2.1 Geometry

Biovessels do not present perfectly circular cross section. In the reference unstressed configuration (subscript 0), the cross section shape is elliptical (ellipticity k_0, ratio of the semi-major axis a_0 to the semi-minor axis b_0). The cross section collapsed configurations are computed from a deformation model of an infinitely long straight floppy tube with a thin homogeneous isotropic and purely elastic wall (Bonis *et al.*, 1981, Ribreau *et al.*, 1993). The transmural pressure is supposed to be uniformly distributed in every tube section and bending effects are assumed to be predominant. The wall thickness is small relative to the wall mid-line curvature radius. The neutral mid-line is deformed without circumferential extension. The tube collapses then according to a bilobal mode. Due to symmetry, a quarter of the wetted perimeter at different collapsed states is displayed in Fig. 1, where 100 points define the wall position. Let S denotes one of the five investigated two-dimensional cross sections (defined by the subscripts 0, q, t, c, ℓ). The point on the y-axis is the mid-face point whereas the point on the x-axis defines the edge. The cross sectional area A and its normalized values $\tilde{A}$, the dimensionless hydraulic diameter $\tilde{d}_h = (4\tilde{A}/\tilde{\chi})(\pi/k_0)$ (χ : wetted perimeter of the cross section) as well as the dimensionless maximum height (ordinate) and width (abscissa) of the cross section of the unstressed ($k_0 = 1.005$) and investigated collapsed tubes are given in Tab. 1 (see section 2.2 for dimensionless variables).

Due to the symmetry of the cross wall with respect to the coordinate axes, only the quarter of the cross section is studied in the positive quadrant ($x \geq 0$, $y \geq 0$) of the Cartesian reference frame $\mathbf{R}(O;\hat{\mathbf{e}}_x,\hat{\mathbf{e}}_y,\hat{\mathbf{e}}_z)$, where O is the point on the z-axis at the inlet cross section and $(\hat{\mathbf{e}}_x,\hat{\mathbf{e}}_y,\hat{\mathbf{e}}_z)$ an orthonormal basis for the space. Apart from $p = 0$, four transmural pressures are of interest: (i) the quasi-ovalisation pressure p_q, (ii) the stream division pressure p_t, the greatest pressure associated with two lateral peak velocities, (iii) the point-contact pressure p_c, the greatest pressure at which the opposite sides touch and (iv) the line-contact pressure p_ℓ, when the radius of curvature at the contact point becomes infinite.

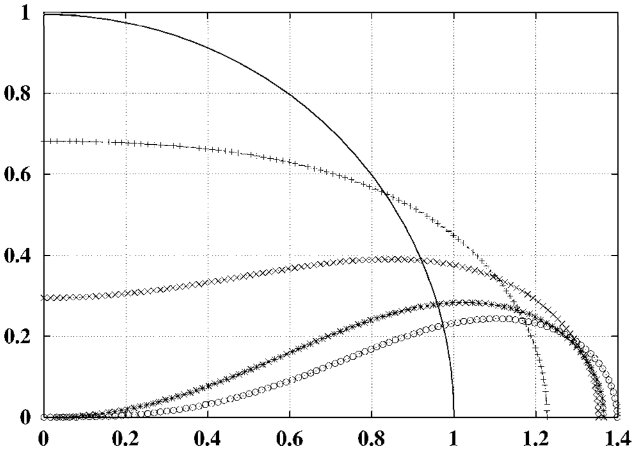

Figure 1 : Unstressed cross section shape S_0 (solid line) and four explored collapsed configurations corresponding to geometrical data given in Tab. 1: S_q (+), S_t (×), S_c (∗), S_ℓ (○).

Table 1 : Bidimensional geometrical data: area A, normalized area $\tilde{A}$, maximum dimensionless cross wall coordinates and dimensionless hydraulic diameter $\tilde{d}_h$ of the investigated cross sections.

variables	S_0	S_q	S_t	S_c	S_ℓ
A	3.12	2.76	1.79	0.84	0.66
$\tilde{A}$	1.00	0.89	0.57	0.27	0.21
$\tilde{x}_M$	1.000	1.228	1.353	1.366	1.398
$\tilde{y}_M$	0.995	0.681	0.390	0.282	0.243
$\tilde{d}_h$	2	1.76	1.14	0.54	0.42

Let s be the arclength along the wall boundary of any cross section S, with the origin at the mid-face. The wall cross line is clockwize oriented. The dimensionless local curvature $\tilde{\kappa}$ *vs.* dimensionless arclength $\tilde{s}$ relationships for the investigated configurations are shown in Fig. 2. In S_0, $\tilde{\kappa}$ is constant and equal to -1. The curvature is indeed defined at the point of the wall mid-line from the angle gradient $d\theta/d\tilde{s}$ where θ is the angle between $\hat{\mathbf{e}}_x$ and the clockwize oriented unit tangent. Along the selected quarter of the wall of S_0, $\theta = -\tilde{s}$, therefore $d\theta/d\tilde{s} = -1$. At mid-face ($\tilde{s} = 0$), the curvature is negative in S_q, is equal to zero in S_ℓ, and is positive in S_t

and S_c. The curvature minimum is observed at the edge whatever Σ; the maximum is located at the mid-face, except in S_ℓ, where it is located near $\tilde{s} = 0.4$.

Σ denotes one of the five three-dimensional fluid domains obtained by a translation of the choosen cross section according to z-axis.

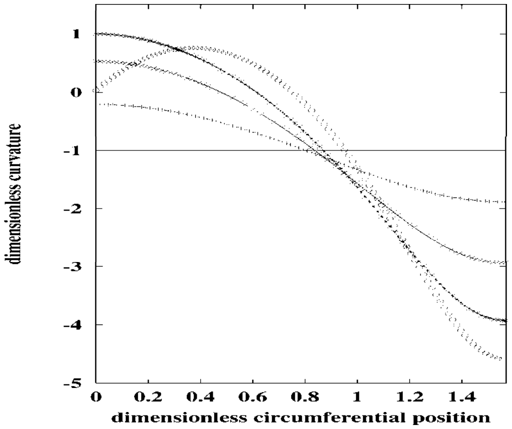

Figure 2 : Relationships between $\tilde{\kappa}$ and $\tilde{s}$ for the unstressed S_0 (solid line) and the four investigated collapsed bidimensional configurations: S_q $(+)$, S_t $(\times)$, S_c $(*)$, S_ℓ $(\circ)$.

2.2 Governing equations

The governing equations of a pipe steady flow are derived from the mass and momemtum conservation:

$$\nabla \cdot \mathbf{u} = 0 \quad ; \quad \rho(\mathbf{u} \cdot \nabla)\mathbf{u} = \mathbf{f} + \nabla \cdot \mathbf{C},$$

where $\mathbf{u}$ is fluid velocity, $\mathbf{f} = -\nabla\Phi$ the body force density (Φ: potential from which body force per unit volume are derived), $\mathbf{C} = -p_i\mathbf{I} + \mathbf{T}$ the stress tensor, $\mathbf{T} = 2\mu\mathbf{D}$ the extra-stress tensor (Newtonian fluid), $\mathbf{D} = (\nabla\mathbf{u} + \nabla\mathbf{u}^T)/2$ the deformation rate tensor, $\mathbf{I}$ the identity tensor, ρ the fluid density and μ the fluid dynamic viscosity (∇, $\nabla\cdot$ and Δ are the gradient, divergence and Laplace operators respectively). The Navier-Stokes equation becomes:

$$\rho(\mathbf{u} \cdot \nabla)\mathbf{u} = -\nabla p_i^\star + \mu\Delta\mathbf{u}, \tag{1}$$

where $p_i^\star = p_i + \Phi$. The pressure notation is simplified in the following sections ($p_i^\star = p_i$).

Scales and dimensionless equations The semi-axis a_0 is used as the transverse and axial length scale. Therefore, the dimensionless perimeter, which is constant in the set of investigated configurations, is given by $\tilde{\chi}_0 = \chi_0/a_0$. Furthermore, the cross sectional area $\tilde{A}$ is normalized with respect to its unstressed value A_0 so that $\tilde{A} = A/A_0$. Normalised coordinates are used in the present paper; for instance, $z^+ = \tilde{z}/\tilde{z}_M = \tilde{z}/\tilde{L}$ (z_M: maximum). The dimensionless kinematic and dynamic variables are obtained from the dimensional quantities using the velocity scale: $\tilde{\mathbf{u}} = \mathbf{u}/V$, $\tilde{p}_i = p_i/(\rho V^2)$. The dimensionless governing equations become:

$$(\tilde{\mathbf{u}} \cdot \tilde{\nabla})\tilde{\mathbf{u}} = -\tilde{\nabla}\tilde{p}_i + Re^{-1}\tilde{\Delta}\tilde{\mathbf{u}}; \quad \tilde{\nabla} \cdot \tilde{\mathbf{u}} = 0. \tag{2}$$

Boundary conditions The boundary of the fluid domain Σ is partioned into three surfaces: the entry cross section Γ_1, the exit cross section Γ_2 and the pipe wall Γ_3. The boundary conditions (BCs) are: $\tilde{\mathbf{u}} \cdot \hat{\mathbf{e}}_z = \tilde{u}_\Gamma$ on Γ_1, $\tilde{\mathbf{C}}\hat{\mathbf{n}}_2 = \mathbf{0}$ on Γ_2, $\tilde{\mathbf{u}} = \mathbf{0}$ on Γ_3, where $\tilde{u}_\Gamma$ is the uniform injection velocity and $\hat{\mathbf{n}}_2$ the outer unit normal vector at Γ_2.

The computations can be performed either with constant axial pressure difference or with constant flow rate, whatever Σ. The present work is linked to experiments with constant flow rate on cell cultures in flow chambers. Let us consider the fully developed steady laminar flow in a straight tube of rigid smooth wall and of circular cross section, *i.e.* the Poiseuille flow, with its axisymmetrical velocity profile $\tilde{u}_z(\tilde{r}) = (1 - \tilde{r}^2)$ ($\tilde{r}$: radial distance from tube axis). The dimensionless flow rate is thus equal to 1/2. The values of $\tilde{u}_\Gamma$ are adjusted to maintain a constant $\tilde{q}$ whatever Σ. Consequently, $\tilde{u}_\Gamma = 1/(2\tilde{A})$. The values of $\tilde{u}_\Gamma$ are given in Tab. 2.

Governing parameter The Reynolds number is defined by the local velocity scale V, the length scale a_0 and the fluid kinematic viscosity ν. Because $\tilde{q} = 1/2$, $V = 2u_\Gamma\tilde{A}$; since χ is constant for the whole Σ set, $Re = Ud_h/\nu$, where U is the cross sectional average velocity. Therefore, $Re = 4q/(\chi\nu)$; Re is invariant whatever Σ. In any Σ, changes in Re are obtained by suitable changes in ν. The numerical tests were carried out for three given Reynolds numbers Re equal to $35, 500$ and 1000. The minimum and maximum values are found in large and medium sized veins of the lower limbs; 500 is an intermediate value.

Wall shear stress The dimensionless extra-stress tensor is equal to $\tilde{\mathbf{T}} = 2Re^{-1}\tilde{\mathbf{D}}$. At each point of the boundary Γ_3 of Σ, the dimensionless dissipative stress vector $\tilde{\boldsymbol{\tau}} = 2Re^{-1}\tilde{\mathbf{D}}\hat{\mathbf{n}}$ associated with the dimensionless extra-stress tensor $\tilde{\mathbf{T}}$ is defined by:

$$\begin{aligned}\tilde{\boldsymbol{\tau}} &= Re^{-1}\Big\{\Big[(2\tilde{u}_{x,x}n_x + (\tilde{u}_{x,y}+\tilde{u}_{y,x})n_y + \\ &\qquad\qquad (\tilde{u}_{x,z}+\tilde{u}_{z,x})n_z\Big]\hat{\mathbf{e}}_x \\ &+ \Big[(\tilde{u}_{x,y}+\tilde{u}_{y,x})n_x + 2\tilde{u}_{y,y}n_y + (\tilde{u}_{y,z}+\tilde{u}_{z,y})n_z\Big]\hat{\mathbf{e}}_y \\ &+ \Big[(\tilde{u}_{x,z}+\tilde{u}_{z,x})n_x + (\tilde{u}_{y,z}+\tilde{u}_{z,y})n_y + 2\tilde{u}_{z,z}n_z\Big]\hat{\mathbf{e}}_z\Big\},\end{aligned}$$

where $\hat{\mathbf{n}}$ is the inner unit normal vector of the boundary Γ_3. $\tilde{u}_x$ is the $\tilde{x}$-component of $\tilde{\mathbf{u}}$ in the Cartesian basis $(\hat{\mathbf{e}}_x, \hat{\mathbf{e}}_y, \hat{\mathbf{e}}_z)$. $\tilde{u}_{x,y}$ is the partial derivative of $\tilde{u}_x$ with respect to $\tilde{y}$. The same notation is used for every vector component and partial derivative.

The dimensionless stress vector $\tilde{\boldsymbol{\tau}}$ is expressed in a local basis. Let $\hat{\mathbf{t}}$ the transverse tangent unit vector, which is perpendicular to $\hat{\mathbf{n}}$ (in straight duct of uniform cross section, it belongs to the plane of the cross section); $\hat{\mathbf{t}}$ is oriented in the anticlockwise direction. Let $\hat{\mathbf{b}} = \hat{\mathbf{t}} \wedge \hat{\mathbf{n}}$; the Frenet trihedron $(P; \hat{\mathbf{n}}, \hat{\mathbf{t}}, \hat{\mathbf{b}})$ is then defined in each point P of Γ_3. $(\tilde{\tau}_t, \tilde{\tau}_n, \tilde{\tau}_b)$ denote the components of the vector $\tilde{\boldsymbol{\tau}}$ in this trihedron. In the local Frenet basis $\tilde{\boldsymbol{\tau}}$ becomes:

$$\begin{aligned}\tilde{\boldsymbol{\tau}} &= J\Big\{[(t_y b_z - t_z b_y)\tilde{\tau}_x + (t_z b_x - t_x b_z)\tilde{\tau}_y \\ &\qquad + (t_x b_y - t_y b_x)\tilde{\tau}_z]\,\hat{\mathbf{n}} \\ &+ [(b_y n_z - b_z n_y)\tilde{\tau}_x + (b_z n_x - b_x n_z)\tilde{\tau}_y \\ &\qquad + (b_x n_y - b_y n_x)\tilde{\tau}_z]\,\hat{\mathbf{t}} \\ &+ [(n_y t_z - n_z t_y)\tilde{\tau}_x + (n_z t_x - n_x t_z)\tilde{\tau}_y \\ &\qquad + (n_x t_y - n_y t_x)\tilde{\tau}_z]\,\hat{\mathbf{b}}\Big\},\end{aligned}$$

where J is the determinant of the Jacobian matrix of the Cartesian-to-Frenet frame change:

$$J = b_x(n_y t_z - n_z t_y) - b_y(n_x t_z - n_z t_x) + b_z(n_x t_y - n_y t_x).$$

2.3 Numerical Method

Three numerical steps are associated with the finite element method: (i) the configurations Σ are meshed, (ii) the Navier-Stokes equations are solved and (iii) the fields of the mechanical quantities are processed.

Mesh generation The quarter of cross section ($\tilde{x} \geq 0$ and $\tilde{y} \geq 0$) is meshed from its boundaries (wall part and segments on axes $\tilde{x} = 0$ and $\tilde{y} = 0$). The wall boundary of the cross section is meshed from the minimum number of 15 points which fits the wall contour drawn from an original set of 100 points. The mesh is composed of a peripheral cell layer of significant thickness in order to avoid a discontinuity between the wall and entry velocity Dirichlet conditions, even in high node density meshes; uniform injection velocity BC is thus associated with high entry WSS.

Once the bi-dimensional mesh, which defines the inlet cross section ($\tilde{z} = 0$), is obtained, a translation according to axis $(O; \hat{\mathbf{e}}_z)$ provides the mesh of the three-dimensional domain with the choosen length $\tilde{L}$ ($\tilde{L} > 30\tilde{d_h}$), taking into account the influence of the exit BC on the flow. Each induced pentahedron is then decomposed into three tetrahedra. The whole meshes of the non-contact configurations (Σ_0, Σ_q and Σ_t) are carried out by two successive symmetry according to $\tilde{x} = 0$ and $\tilde{y} = 0$ planes. The meshes of Σ_c and Σ_ℓ are performed by a single symmetry operation according to the $\tilde{y} = 0$ plane. The computations in the contact configurations are only made on the $\tilde{x} \geq 0$ space. The cross sections are thus identical thoughout the whole length of each Σ. Moreover, numerical artifacts due to the mesh asymmetry are avoided. Geometrical and mesh characteristics are respectively given for each Σ in Tab. 2.

Table 2 : Mesh features, dimensionless tube length and inlet boundary condition used to obtain a dimensionless volume flow-rate equal to 1/2 whatever Σ.

Σ	node number	element number	$\tilde{L}$	$\tilde{u}_\Gamma$
Σ_0	17885	96768	84.0	0.50
Σ_q	16219	86976	74.8	0.56
Σ_t	16709	86976	80.0	0.87
Σ_c	8460	43188	67.5	1.85
Σ_ℓ	9150	45720	67.7	2.38

Numerical solution of the governing equations The numerical solution of the Navier-Stokes equations for incompressible fluids is based on a variational formulation of the governing equations:

$$\mathcal{B}(\mathbf{u},\mathbf{v})+\mathcal{T}(\mathbf{u};\mathbf{u},\mathbf{v})+\mathcal{B}'(\mathbf{v},p)=< l,\mathbf{v} >, \quad \forall \mathbf{v}\in V \subset H^1(\Sigma)^3,$$

$$\mathcal{B}'(\mathbf{u},q)=0,\ \forall q \in Q \subset L^2(\Sigma)$$

where $\mathcal{B}$ et $\mathcal{B}'$ are bilinear forms, $\mathcal{T}$ a trilinear form, $< l,\mathbf{v} >$ the dual product (the quantity l takes into account the nonhomogeneous velocity and possible pressure BCs as well as the possible forcing term $\mathbf{f}$), $H^1(\Sigma)$ and $L^2(\Sigma)$ the Sobolev spaces of order 1 defined on Σ for vector-valued functions and the space of functions that are square integrable in the Lesbegue sense with respect to Σ respectively.

The discretization uses finite elements defined by a Lagrange interpolation; the pressure and the velocity are computed in P1/P1isoP2 tetrahedra (Glowinski, 1984). The computational method is suitable for unsteady flow. In steady flow, the time acts as iteration parameter until convergence, *i.e.* until the norms provided with the classical Hilbert spaces of the difference between two successive iterations of the pressure and velocity fields is constantly below a given tiny threshold. The time discretization uses a fractional step scheme of order 2 (Boukir *et al.*, 1992). The convection step is processed by a characteristic method (Pironneau, 1982). The diffusion step is based on the Chorin-Temam method. The linear system is solved using the conjugate gradient method.

Computation of the dissipative stress vector The dissipative stress vector $\tilde{\boldsymbol{\tau}}$ is computed using the nodal values of the velocity in each tetrahedron and an interpolation by Lagrange polynomials of degree one. The viscous component of the stress tensor is thus constant in each tetrahedron; $\tilde{\boldsymbol{\tau}}$ is then constant on each face of the tube wall Γ_3. $\tilde{\boldsymbol{\tau}}$ is computed at each node of Γ_3 using a weighting factor which is the area of the corresponding triangle.

3 Results

Longitudinal pressure difference The fluid is conveyed in straight tubes; consequently, the so-called pressure p_i is uniform throughout any cross section. The pressure differences $\delta\tilde{p}$ between the tube inlet and outlet, where the pressure is set to zero, are given in each Σ for the three values of *Re* in Tab. 3. Since q is constant, the higher the Reynolds number the smaller the pressure difference for a given Σ (Fig. 3). The pressure variations along the tube axis are non-linear in the entrance region whereas they are linear in its downstream segment. Whereas $\tilde{A}$ decreases from 1 to 0.21, $\delta\tilde{p}$ is multiplied by a factor of about 45 at high *Re* and about 50 at low *Re*.

Table 3 : Pressure differences between the tube inlet and outlet for the same flow rate (zero exit p_i).

Re	35	500	1000
Σ_0	9.5	0.78	0.45
Σ_q	12.5	1.02	0.58
Σ_t	57.9	4.26	2.26
Σ_c	277.1	21.14	12.00
Σ_ℓ	489.4	37.45	20.52

Velocity field Velocity profiles in the planes $(O;\hat{\mathbf{e}}_x,\hat{\mathbf{e}}_z)$ and $(O;\hat{\mathbf{e}}_y,\hat{\mathbf{e}}_z)$ at selected axial stations are displayed rather than velocity distributions in the whole cross section in order to compare easily in one plot the axial velocity changes, for each Σ at given *Re*. The boundary layer develops in the streamwise direction from the entrance cross section since the inlet boundary conditions is defined by an uniform injection velocity. The velocity profiles remain similar after a given length, the so-called entrance or entry length; the flow is then fully developed and corresponds to the solution of Ribreau *et al.* (1994).

Entry length The dimensionless entry length ($\tilde{L}e$) of a laminar flow in an axially uniform straight rigid duct is, in the present work, defined using a relative velocity index with a threshold of 0.05. The relative velocity index $(\tilde{u}_M-\tilde{u}_z)/\tilde{u}_M$ is computed from the dimensionless velocity maximum $\tilde{u}_M$ at $Re = 35$: indeed, at low *Re*, the flow is fully developed downstream from a short entry length. Moreover for a given Σ, the velocity profiles are the same whatever *Re* because $\tilde{q}$ is constant.

The dimensionless entry length $\tilde{L}e$ and its normalized values $\tilde{L}e/\tilde{L}$ are given for each Σ and each *Re* in Tab. 4. The smaller the Reynolds number the shorter the entry length for a given Σ (Fig. 4). For a given *Re*, $\tilde{L}e$ is

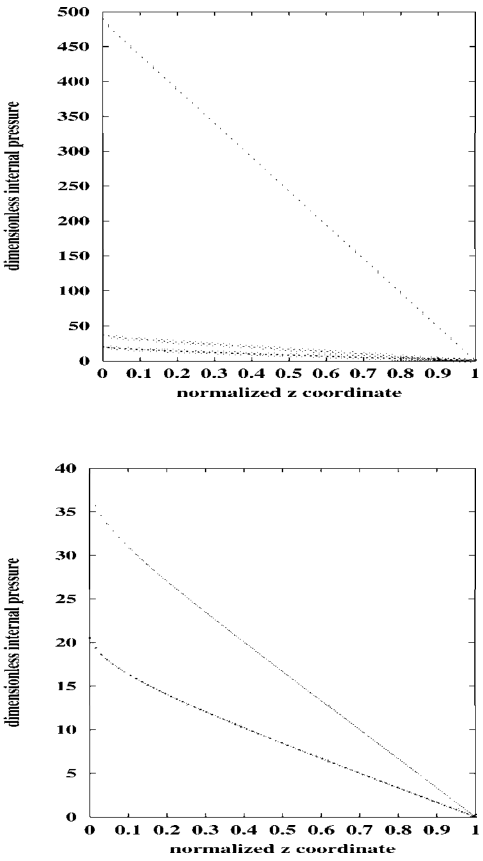

Figure 3 : Top: pressure variations along the axis of Σ_ℓ for the three values of *Re*: 35 (+), 500 (×) and 1000 (∗). Bottom: same as top for $Re = 500$ and 1000 in order to display the non-linearity of the pressure change in the entry region of the tube in its contact configuration.

divided by a factor of about 2 between Σ_0 and Σ_q in the one hand and Σ_t, Σ_c and Σ_ℓ in the other hand, except for Σ_ℓ at $Re = 35$. The ratio $\tilde{Le}/\tilde{L}_m$ is used to estimate the entry length for comparison between the studied Σ, where $\tilde{L}_m$ is the dimensionless length of Σ_c ($\tilde{L}_m$ is the shortest length of our tube set). The smallest values of this ratio are obtained in Σ_t whatever the investigated values of *Re*.

Table 4 : Dimensionless entry length ($\tilde{Le}$) and normalized entry length ($\tilde{Le}/\tilde{L}$), estimated from a velocity index with a threshold of 0.05. For comparison purpose, a ratio ($\tilde{Le}/\tilde{L}_m$) is also given.

Re		35	500	1000
Σ_0	$\tilde{Le}$	2.8	31.6	63.1
	$\tilde{Le}/\tilde{L}$	0.03	0.38	0.75
	$\tilde{Le}/\tilde{L}_m$	0.04	0.47	0.94
Σ_q	$\tilde{Le}$	2.8	31.8	62.1
	$\tilde{Le}/\tilde{L}$	0.04	0.43	0.83
	$\tilde{Le}/\tilde{L}_m$	0.04	0.47	0.92
Σ_t	$\tilde{Le}$	1.60	12.9	24.9
	$\tilde{Le}/\tilde{L}$	0.02	0.16	0.31
	$\tilde{Le}/\tilde{L}_m$	0.02	0.19	0.37
Σ_c	$\tilde{Le}$	1.70	16.6	31.9
	$\tilde{Le}/\tilde{L}$	0.03	0.25	0.47
	$\tilde{Le}/\tilde{L}_m$	0.03	0.25	0.47
Σ_ℓ	$\tilde{Le}$	3.1	15.7	30.6
	$\tilde{Le}/\tilde{L}$	0.05	0.23	0.45
	$\tilde{Le}/\tilde{L}_m$	0.05	0.23	0.45

Configurations without contact In the vicinity of the entrance section, the velocity profile exhibits a plateau in the core region and high velocity gradient near the wall, due to the imposed inlet boundary condition. Further downstream from the entrance section, a velocity maximum is observed for every axial stations on Σ_q axis (Fig. 5). When the opposite walls are concave (Σ_t), the velocity maximum migrates laterally where the tube lumen is the largest (Fig. 6).

Contact configurations In contact configurations, the velocity field is explored in the part of the tube lumen located in the space $\tilde{x} \geq 0$. The lumen region near the contact point is characterized by a very low velocity flow. The results are displayed for $Re = 1000$. Let us decompose the $\tilde{x}$-coordinate of the investigated part of the cross section in 4 zones: (i) zone I where the velocity which is nearly equal to zero ($0 \leq \tilde{x} \leq 0.20$ for Σ_c and $0 \leq \tilde{x} \leq 0.29$ for Σ_ℓ), (ii) zone II where the velocity increases up the left 'intersection point' of the velocity profiles ($0.20 \leq \tilde{x} \leq 0.64$ for Σ_c and $0.29 \leq \tilde{x} \leq 0.75$ for Σ_ℓ), (iii) zone III where the velocity either displays a plateau or reaches its maximum ($0.64 \leq \tilde{x} \leq 1.23$ for Σ_c and $0.75 \leq \tilde{x} \leq 1.29$ for Σ_ℓ) and (iv) zone IV near the outer edge, of small thickness, where the velocity decreases to satisfy the no-slip condition, as shown in Fig. 7. The axial velocity gradient in zone II decreases significantly downstream, whereas the speed axial variations in zone III are very small. The tube length over

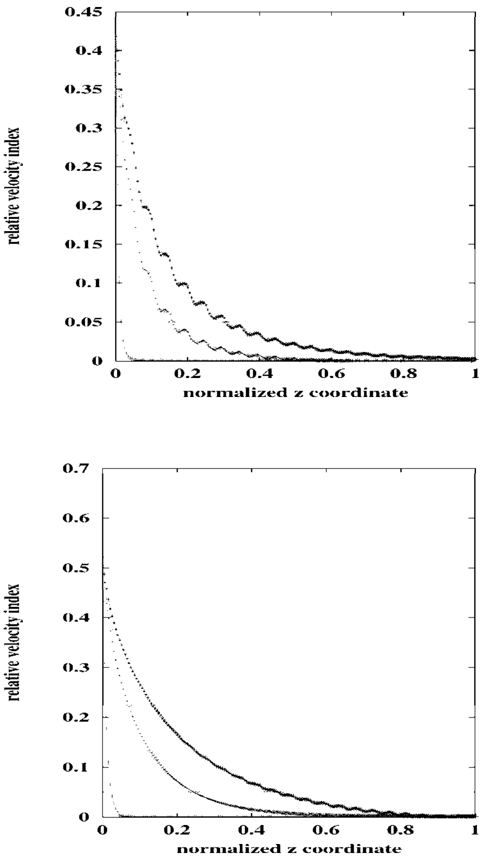

Figure 4 : Variations of the velocity index in Σ_t (top) and in Σ_c (bottom) for the three *Re*: 35 (+), 500 (×) and 1000 (∗). The solid line defines the 5 per cent arbitrary choosen threshold.

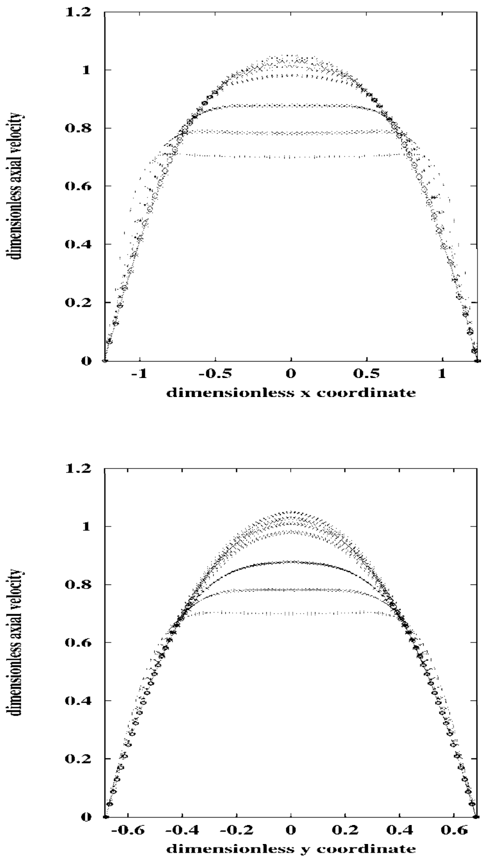

Figure 5 : Velocity profile in the centerplane (top) and in the plane normal to the centerplane at the tube axis (bottom) of Σ_q when $Re = 1000$ at selected axial stations z^+: 0.0 (solid line), 0.07 (+), 0.13 (×), 0.27 (∗), 0.53 (○), 0.67 (△), 0.80 (▽), 0.99 (◇).

which the velocity profiles display a plateau is great, especially for large *Re*. The velocity profiles are displayed in one axial station $z^+ \sim 0.04$ $(\tilde{z}/\tilde{d}_h \sim 11.5)$ of Σ_ℓ $(z^+ = \tilde{z}/\tilde{L})$, for the three *Re* in Fig. 8. The higher *Re* the higher the slope of the velocity profile near the contact point. Further downstream from the entrance section, a velocity maximum is observed for every axial stations along a line parallel to the tube axis and through the point $(\tilde{x} \sim 0.96, \tilde{y} = 0)$ for Σ_c and $(\tilde{x} \sim 1.1, \tilde{y} = 0)$ for Σ_ℓ.

Wall shear stress $\tilde{\tau}_b = \tilde{\tau}_z$ because the cross section is axially uniform. In fully-developed steady laminar flow in long uniform ducts of smooth rigid walls and of circular cross sections, the so-called Poiseuille flow, the wall shear stress is constant throughout the whole tube, in the streamwize direction as well as along the wetted perimeter. Because, in such a flow, $\tilde{\tau}_b \times Re = 2$, $\tilde{\tau}_b \times Re$ is taken here as the variable of interest.

Configurations without contact The variation in $\tilde{\tau}_b \times Re$ along $\tilde{s}$ at selected cross sections is plotted in Fig. 9 when $Re = 1000$ for Σ_q and Σ_t respectively. In Σ_q, WSS maxima are located at mid-faces $(\tilde{s} = 0)$, whatever the axial station, whereas $\tilde{\kappa}$ is maximum. WSS minima are observed at both edges $(\tilde{s} \sim \pi/2)$ where $\tilde{\kappa}$ is minimum. For a given $\tilde{s}$, the WSS differences between the tube entrance region and the downstream segment is the smallest at both mid faces and the greatest at both edges. The WSS increases with *Re* without appreciable change in the cross variations at given axial stations. In Σ_t, the WSS decreases from its maximum located in the

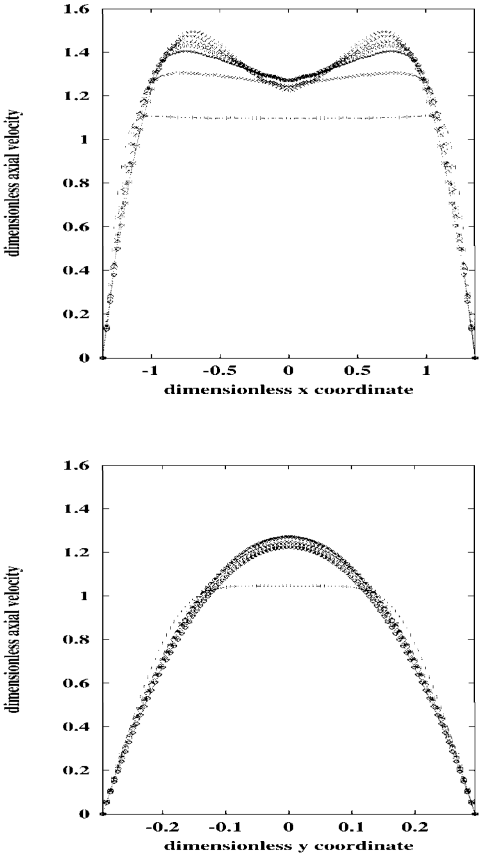

Figure 6 : Velocity profile in the centerplane (top) and in the plane normal to the centerplane at the tube axis (bottom) of Σ_t when $Re = 1000$ at selected z^+: 0.0 (solid line), 0.05 ($+$), 0.13 ($\times$), 0.23 ($*$), 0.33 ($\circ$), 0.50 ($\triangle$), 0.75 ($\bigtriangledown$), 0.88 ($\diamond$).

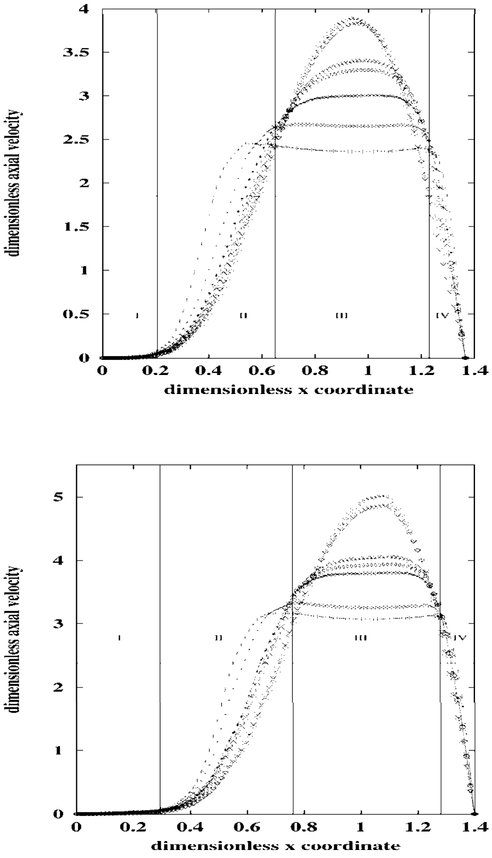

Figure 7 : Velocity profile in the centerplane at $Re = 1000$. Top: in Σ_c at z^+: 0.0 (solid line), 0.03 ($+$), 0.07 ($\times$), 0.13 ($*$), 0.22 ($\circ$), 0.27 ($\triangle$), 0.71 ($\bigtriangledown$), 0.94 ($\diamond$). Bottom: in Σ_ℓ at z^+: 0.0 (solid line), 0.03 ($+$), 0.04 ($\times$), 0.11 ($*$), 0.13 ($\circ$), 0.16 ($\triangle$), 0.53 ($\bigtriangledown$), 0.95 ($\diamond$). Four zones are defined in the developing velocity profiles (see text).

middle of the face to its minimum at the edge.

Contact configurations The magnitude of the WSS is much greater than in configurations without contact whatever the axial station. The variation in $\tilde{\tau}_b \times Re$ along $\tilde{s}$ at selected $\tilde{z}$ is plotted in Fig. 10 for Σ_c and Σ_ℓ. In quarter S (space $\tilde{x} \geq 0, \tilde{y} \geq 0$), the cross variation in wall shear stress is defined by three extrema. The WSS is equal to zero at the contact point. A second minimum occurs at the edge, while a maximum appears at a point of the face. The maximum moves from $\tilde{s} \sim 0.5$ in the entrance segment ($z^+ = 0.03$) to $\tilde{s} \sim 0.9$ in the downstream segment ($z^+ = 0.27$) in Σ_c; it migrates from $\tilde{s} \sim 0.65$ at $z^+ = 0.03$ to $\tilde{s} \sim 0.87$ at $z^+ = 0.53$ in Σ_ℓ. The ratio between the edge minimum and the face maximum is the same in both contact configurations (0.63 at $Re = 1000$). The higher Re, the closer to the contact point the location of the WSS maximum (Fig. 11). Fig. 11 shows that the WSS circumferential variations with Re are superimposed at $z^+ = 0.53$, *i.e.* downstream from the entry length. In the entrance region, the magnitude of the maximum increases when Re rises. This result is in agreement with the slope of the velocity traces exhibited in zone II (Fig. 8).

Axial variations of $\tilde{\tau}_b \times Re$ for a set of given $\tilde{s}$ (iso$\tilde{s}$

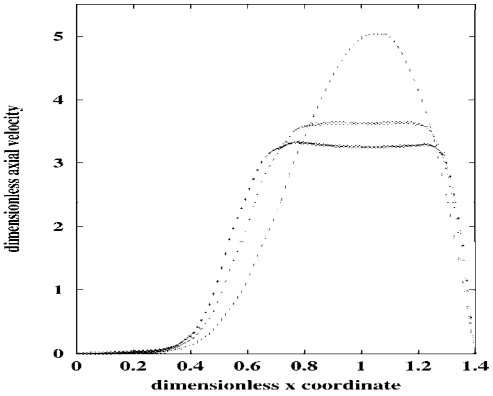

Figure 8 : Velocity profile in the centerplane of Σ_ℓ at $z^+ = 0.04$. $Re = 35$ (+), 500 (×) and 1000 (∗).

$\tilde{\tau}_b \times Re$ *vs.* $\tilde{z}$ relationships) show that the WSS, like the velocity, decreases over a more or less long tube segment according to Re and reaches a value at $\tilde{z} = \tilde{L}e$ which is constant throughout the entire segment of the duct downstream from the entry length: the $\tilde{s}$-set fully developed-flow WSS (SFDFWSS) value. The SFDFWSS depends on $\tilde{s}$ whatever Σ. In Σ_q, the cross-sectional wall remaining concave, the greater the arc length the lower the SFDFWSS, as expected from the iso$\tilde{z}$ $\tilde{\tau}_b \times Re$ *vs.* $\tilde{s}$ relationships plotted in Fig. 9. In configurations caracterized by a change in cross wall curvature from a convex wall to a concave wall, the iso$\tilde{s}$ $\tilde{\tau}_b \times Re$ *vs.* $\tilde{z}$ curves are not sorted according to $\tilde{s}$. In contact configurations, the greater the arc length the greater the SFDFWSS in the wall part associated with small $\tilde{s}$ (regions I and, partially, II depicted in Fig. 10) whereas the greater the arc length the lower the SFDFWSS in the wall part associated with high $\tilde{s}$ (regions III and IV of Fig. 10).

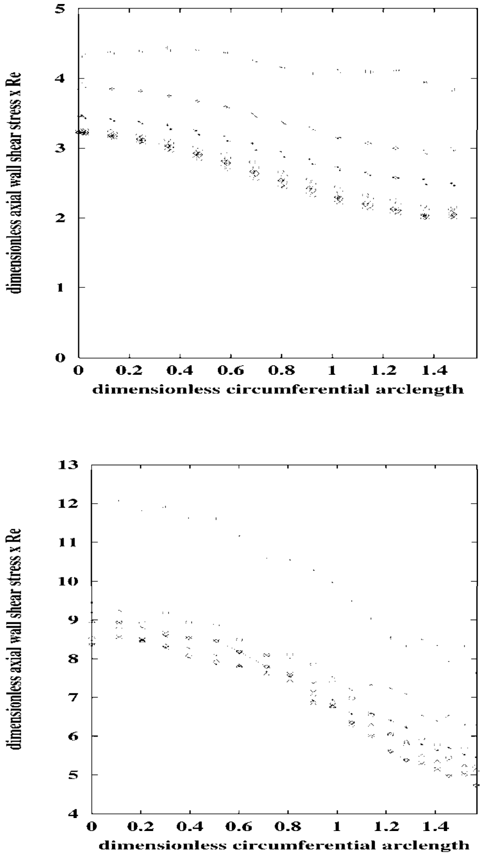

Figure 9 : Wall shear stress $\tilde{\tau}_b \times Re$ when $Re = 1000$ along one forth of the dimensionless wetted cross perimeter from the mid-face (left) to the edge (right). Top: in Σ_q at z^+: 0.07 (+), 0.13 (×), 0.27 (∗), 0.53 (○), 0.67 (△), 0.80 (▽), 0.99 (⋄). Bottom: in Σ_t at z^+: 0.05 (+), 0.13 (×), 0.23 (∗), 0.33 (○), 0.50 (△), 0.75 (▽), 0.88 (⋄).

4 Discussion

The stress exerted on the pipe wall by the flowing fluid is the main variable of interest of the present study. A mixed formulation could be more appropriate to control the accuracy of the WSS computation, especially in the case of flow-induced evolution of the fluid microstructure with more or less memory effects. The usual velocity-pressure formulation is used because the fluid is here assumed to be Newtonian.

The whole set of numerical simulations has been carried out with a constant flow rate and zero pressure at the tube outlet. In the momemtum equation 2, the pressure term is balanced by the difference between the diffusion term and the inertia term. The greater the Reynolds number, the smaller the diffusion term and, consequently the lower the pressure gradient, in particular downstream from the entry length, where the convective term is equal to zero.

While the finite element method is used in the present work, the emergence of "meshless method" to solve the Navier-Stokes equations may alleviate some of the difficulties associated with the finite element methods (*e.g.* Atluri and Shen, 2002). Vortex methods offer also an alternative method for numerical solutions of the Navier-

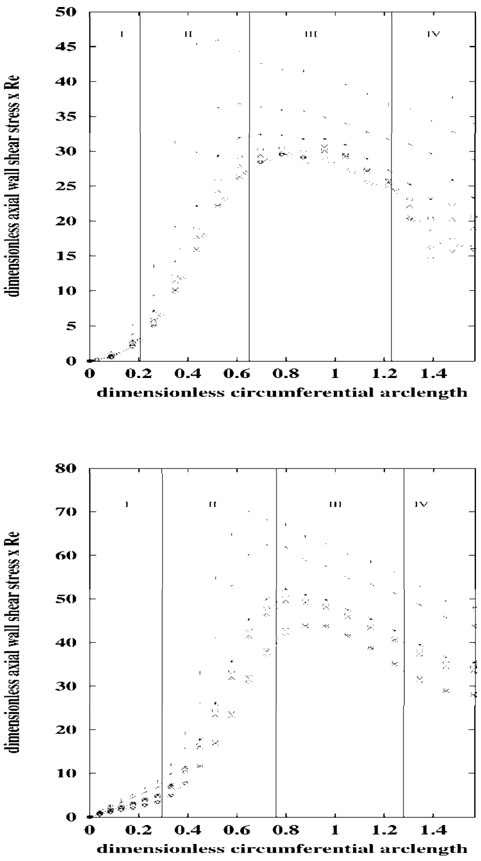

Figure 10 : Wall shear stress $\tilde{\tau}_b \times Re$ when $Re = 1000$ along $\tilde{s}$. Top: in Σ_c at z^+: 0.03 ($+$), 0.07 ($\times$), 0.13 ($*$), 0.22 ($\circ$), 0.27 ($\triangle$), 0.71 ($\bigtriangledown$), 0.94 ($\diamond$). Bottom: in Σ_ℓ at z^+: 0.03 ($+$), 0.04 ($\times$), 0.11 ($*$), 0.13 ($\circ$), 0.16 ($\triangle$), 0.53 ($\bigtriangledown$), 0.95 ($\diamond$). Regions I to IV correspond to the velocity-profile zones of Fig. 7.

Stokes equations; in particular, such a numerical tool may be used for simulations of incompressible viscous flows (*e.g.* Cottet and Koumoutsakos, 2000).

Test validation Result validation and error estimation may be done using the quasi-circular cross sectional configuration Σ_0 for which the analytical solution of the Poiseuille flow gives $\tilde{\tau}_b \times Re = 2$. The maximal relative error obtained in Σ_0, when the flow is fully developed, whatever *Re*, of the WSS computation is about 4% with respect to the theoretical solution.

For each Σ, the tetrahedron number has been multiplied by a factor of about 4 from a low element density mesh. The bulk flow properties remains unchanged; the mesh effects have been considered negligible.

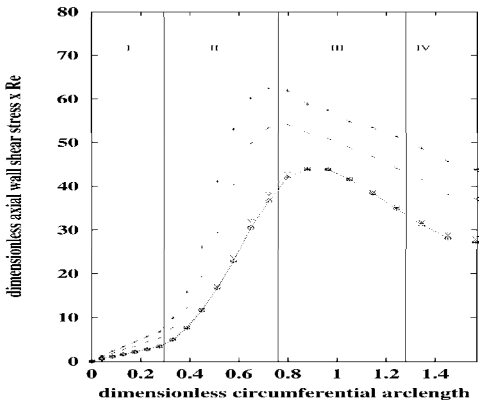

Figure 11 : Wall shear stress $\tilde{\tau}_b \times Re$ in Σ_ℓ along $\tilde{s}$ at two z^+, 0.04 and 0.53, and three *Re*: 35 ($+$ and $\circ$ respectively), 500 ($\times$ and $\triangle$ respectively) and 1000 ($*$ and $\bigtriangledown$ respectively). Regions I to IV correspond to the velocity-profile zones of Fig. 7.

Besides, two finite element techniques were used. The method of the commercial N3S package (EDF-Simulog, France) is described in section 2. The INRIA NSI3 software is based on P1 bubble P1 tetrahedra. The pressure $\tilde{p}_i$ is defined at the four vertices of the tetrahedron (P_1 element) and the velocity $\tilde{\mathbf{u}}$ at both the vertices and the barycenter (P_1 bubble element). The order of the method is $O(\xi^2)$ for $\tilde{\mathbf{u}}$ and $O(\xi)$ for $\tilde{p}_i$ in the L^2 norm, ξ being the characteristic size of the tetrahedron (Arnold *et al.*, 1984). The solution is obtained via a generalized Uzawa-preconditioned-conjugate gradient method (Glowinski, 1984). In both case, the time acts as an iteration parameter for convergence, and the convection step is processed by a characteristic method. The flow behaviour is similar for given flow conditions associated with the same boundary conditions. In particular, the entry length is the same (the plots of the streamwize variations in fluid velocity are similar). The mean relative difference over the whole mesh node set between the two computational velocity fields, the quantity of interest from which both the entry length and the wall shear stress are computed, obtained with N3S and NSI3 softwares, is lower than 4% and the maximum relative difference is lower than 9%.

Entry length The normalized entry length $\tilde{L}e/\tilde{L}$ is given in Tab. 4 for the set of studied configurations. In Σ_ℓ, $\tilde{L}e/\tilde{L} = 0.23$ and 0.25 when $Re = 500$ and 1000 respectively. These normalized streamwize coordinates correspond to the stations at which the pressure plots displayed in Fig. 3 lose their curvilinear shape to become linear. The pressure evolution is thus in agreement with the variation of the velocity index aimed at determining the entry length.

The dimensionless entry length are also computed using different formulas $\tilde{L}e/\tilde{d}_h$ ($\tilde{d}_h$ is given in Tab. 1) and $\tilde{L}e/(\tilde{d}_h.Re)$ for comparison with the literature data (Tab. 5). Note that such expressions must be provided with the cross-sectional shape otherwize the geometry influence may be overlooked. When $Re = 35$, $\tilde{L}e/\tilde{d}_h$ of Σ_0 is multiplied by a factor of about 2.3 and about 5.3 in Σ_c and in Σ_ℓ respectively. $\tilde{L}e/(\tilde{d}_h.Re)$ is nearly constant when $Re \geq 500$ for a given Σ. It takes its highest values for the smallest investigated values of Re ($Re = 35$) whatever Σ, whereas it remains nearly constant when $Re \geq 500$. When $Re \geq 500$, the values of $\tilde{L}e/(\tilde{d}_h.Re)$ in Σ_c and in Σ_ℓ are about 2 and about 2.3 times greater than the values in Σ_0 respectively. The ratio between its values at high Re and at low Re depends on the cross-sectional configuration. It is almost constant for Σ_0 and Σ_q (0.78 and 0.79 respectively) and is equal to 0.5, 0.67 and 0.33 for Σ_t and Σ_c, and Σ_ℓ.

Textbook data provide usually the entry length in a straight duct of circular cross section (Appendix Appendix A), with a huge between-author variability. In Σ_0, $\tilde{L}e/\tilde{d}_h \sim 1.4$ when $Re < 100$ and $\tilde{L}e/(\tilde{d}_h.Re) \sim 0.03$ when $Re > 200$ are close and equal respectively to the most common values proposed in the literature (1.2 and 0.03 respectively).

Biological implications The present work deals with the interaction between flow and cultured cells in pipes. Geometrical and dynamical similarity criteria can be applied between the bioconduit and the experimental duct. However such principles can not be used for the living cells in culture in the flow chamber. The shear stresses applied to the ECs *in vitro* must be the same in magnitude and in direction than the ones experienced by the ECs *in vivo*. When the flow is fully developed and when the flow rate is kept constant, the WSS scale is given by $\mu q/a_0^3$ (Ribreau and Thiriet, 1998, Thiriet *et al.*, 2001). Same WSS are obtained if the criterion $\mu q/a_0^3 = cst$. is satisfied. Knowing the ratio between the test fluid viscosity and the Newtonian value of the blood viscosity in the one hand and the venous flow rate in the other hand, the experimental flow rate can then be deduced, when the flow rate in the test section is fully developed.

Table 5 : Two other usual expressions of the dimensionless entry length ($\tilde{L}e/\tilde{d}_h$, $\tilde{L}e/(\tilde{d}_h.Re)$).

	Re	35	500	1000
Σ_0	$\tilde{L}e/\tilde{d}_h$	1.4	15.8	31.6
	$\tilde{L}e/(\tilde{d}_h.Re)$	0.04	0.03	0.03
Σ_q	$\tilde{L}e/\tilde{d}_h$	1.6	18.1	35.3
	$\tilde{L}e/(\tilde{d}_h.Re)$	0.05	0.04	0.04
Σ_t	$\tilde{L}e/\tilde{d}_h$	1.4	11.3	21.9
	$\tilde{L}e/(\tilde{d}_h.Re)$	0.04	0.02	0.02
Σ_c	$\tilde{L}e/\tilde{d}_h$	3.2	30.7	59.1
	$\tilde{L}e/(\tilde{d}_h.Re)$	0.09	0.06	0.06
Σ_ℓ	$\tilde{L}e/\tilde{d}_h$	7.4	37.4	72.9
	$\tilde{L}e/(\tilde{d}_h.Re)$	0.21	0.07	0.07

Geometrical data of large and medium-sized veins of the systemic circulation are given in Tab. 6. Haemodynamic quantities in the same veins are either provided by the literature data or computed from d_h with a blood kinematic viscosity ν of $4.10^{-6} m^2.s^{-1}$ (Tab. 7). There is a large between-subject variability in vein size and flow for a given vein in healthy subject. Subject position and activity (rest / exercise) affect the vein size. For instance, the flow rate in the common femoral vein of a lying atheletic young male at tidal respiration is equal to about 230 $ml.mn^{-1}$ (vein diameter: 5 mm) while it is equal to about 150 $ml.mn^{-1}$ (vein diameter: 16 mm) in the same standing subject. The provided WSS values are thus only estimates (Tab.8).

In large and medium sized blood vessels, where the ratio between the vessel-flow length scale and the characteristic size of the circulating cells is quite small, RBCs are not expected to deform. In large blood vessels, when RBCs have undergone a stress history such that there is no residual RBC agregates and when the convection time

Table 6 : Usual hydraulic diameter at $p = 0$ and perimeter of cross section of selected veins supposed to have circular cross section in normal adults in lying position.

Vein	d_h (mm)	χ (mm)
Vena cava	25	78.5
Common femoral	9	28.3
Posterior tibial	4	12.6

Table 7 : Estimated cross sectional average velocity U, volume flow rate q and Reynolds number Re in some selected veins.

Vein	q (ml/s)	U (m/s)	Re
Vena cava	75	0.15	955
Common femoral	2	0.03	71
Posterior tibial	0.08	0.006	6

scale is greater than the agregation time scale, the blood is supposed to be Newtonian. This assumption is relevant in open configurations Σ_0, Σ_q and Σ_t. However, in the contact configurations Σ_c and Σ_ℓ, the flow region near the contact point is characterized by a slow flow. In the present work, the agregation time constant, supposed to be greater than the platelet one, is assumed to be higher than the local convective time scale. The convective time scale is supposed to be higher than in a flow separation region, where the fluid is recirculating with a low speed, especially near the pipe wall, or in a lateral cavity, like arterial aneurisms, where the viscous effects induce less driving forces on the fluid than in a slow flow region of the vessel lumen. RBC agregation, which might occur in flow stagnation regions, is expected to be inhibited in the very low shear region located in the vessel lumen near the wall contact. Any RBC rouleau network, which appears in rest blood, are indeed distroyed into small rouleaux at very low shears ($\dot{\gamma} = 10^{-2}\,s^{-1}$).

5 Conclusion

Flow chambers made of channels with cell-coated walls are aimed at exploring the mechanotransduction properties of endothelial cells of the interface between the blood and the vessel wall. The wall shear stress has been found to trigger changes in shape, density, rate

Table 8 : Wall shear stress (WSS) extrema (minimum WSS_m and maximum WSS_M in *Pa*) and maxima of its cross- (WSScg_M) and axial (WSSag_M) gradient ($Pa.m^{-1}$) estimated in systemic veins from the computational model results.

Vein Re	Vena cava 1000	Common femoral 35	Posterior tibial 35
Σ_0			
WSS_m	0.2	0.2	0.01
WSS_M	0.3	0.4	0.02
WSScg_M	0.	0.	0.
WSSag_M	0.4	1.4	0.1
Σ_q			
WSS_m	0.2	0.2	0.01
WSS_M	0.4	0.5	0.02
WSScg_M	6.4	21.6	2.0
WSSag_M	0.8	2.7	0.3
Σ_t			
WSS_m	0.4	0.5	0.02
WSS_M	1.1	1.4	0.05
WSScg_M	18.3	61.6	5.7
WSSag_M	1.5	5.0	0.5
Σ_c			
WSS_m	2.0	2.4	0.1
WSS_M	4.4	5.3	0.2
WSScg_M	630.	2380.	220.
WSSag_M	7.7	25.6	2.1
Σ_ℓ			
WSS_m	2.9	3.5	0.1
WSS_M	5.9	7.2	0.3
WSScg_M	629.	2110.	195.
WSSag_M	6.7	22.5	2.1

division and biochemical syntheses of the endothelial cells. The field of the wall shear stress induced by an homogeneous Newtonian incompressible fluid which flows steadily with given Reynolds numbers is here investigated in collapsed tubes of axially uniform cross sections. Such cross section shapes are associated with tranverse variations in the longitudinal component of the wall shear stress. Consequently, in addition to the pressure, the cell is subjected not only to a shear force but also to a shear torque at its inertia center.

The cross section shape affects significantly the distribution of the wall shear stress along the wetted tube perimeter. Variations in the wall shear stress are greater when the opposite walls of the cross section are in contact. Moreover, the higher the Reynolds number and/or the closer the station from the entry section, the greater the variation range of the cross distribution of the wall shear stress. The results can be used to design flow chambers composed of a collapsed pipe to introduce cross effects. Cell adherence to the conduit wall, tissue cohesion, shape and functions can then be tested by a local two-component force, which is closer to the *in vivo* conditions. Moreover, the present results are necessary to interpret the data collected during biological observations and measurements on cell cultures in such flow chambers.

Acknowledgement: The authors are grateful to a referee for his very useful comments.

Appendix A: Entry length

The entry length *Le* (or entrance length or inlet length), of a steady flow, whatever its regime, in any pipe, is the distance between the inlet section and the station from which the flow profile does not change. More precisely, for a steady laminar flow in a long straight cylindrical conduit of circular cross section and smooth rigid impermeable wall, with uniform injection velocity for instance, the entry length is the pipe length from which the deviation of the velocity distribution from the Poiseuille distribution is less than 1 percent (Boussinesq, 1891). The viscous effects have then pervaded the whole tube lumen. The inlet length has also been defined, for an easier record, as the distance through which the developing maximum velocity, which is the centerline velocity in a long straight tube, reaches 99 percent of the peak velocity of the fully developed flow.

Boussinesq (1891) proposed $Le/(d_h.Re) = 0.065$ through which the velocity is redistributed approximately into a parabolic profile[3]. However, this value is overestimated, and the following value is proposed[4]: $Le/(d_h.Re) \sim 0.015$ when $200 < Re < 2500$. When[5] $Re < 200$, $Le/d_h = 1.2$. The entry length can also be calculated using literature formulae from *Re* and a set of fitting constants; the calculated quantity is either *Le*[6] or Le/d_h, using either a linear[7] or a meromorph equation[8]. For a single and simple investigated flow as the laminar steady flow in a long uniform straight pipe with rigid smooth wall and circular cross section, there is a range of available data and not a single value.

Reference

Arnold, D.N.; Brezzi, F.; Fortin, M. (1984): A stable finite element for the Stokes equations. *Calcolo*, vol. 21, pp. 337-344.

Atkinson, B.; Brocklebank, M.P.; Card, C.C.H.; Smith, J.M. (1969): Low Reynolds number developing flows. *Am. Inst. Chem. Eng. J.*, vol. 15, pp. 548-553.

Atluri, S.N.; Shen, S. (2002): *The Meshless Local Petrov-Galerkin (MLPG)*, Tech Science Press, CA.

---

[3] An approximate analysis from the estimation of the boundary layer thickness gives a similar result: $\delta \sim 2(\nu z/U)^{1/2}$, therefore $Le/(d_h.Re) = 0.0625$. A value of 0.06 is given in many textbooks (*e.g.* Comolet, 1976, Janna, 1998, Padet, 1991, Shames, 1992). The formulae use either the tube diameter or the radius in the one hand and a Reynolds number based either on the diameter or the radius in the other hand; sometimes both length scales are simultaneoulsly used. The values, based on a single scale, the tube diameter, are thus here modified.

[4] The fluid mechanics literature shows a great between-author data variability *e.g.* 0.01 (Mc Donald, 1974), more suitable for oscillatory flow, 0.028-0.030 (Schiller, 1922, Goldstein, 1938, Langhaar, 1942, Sparrow *et al.*, 1964, Fediaevski *et al.*, 1974, Caro *et al.*, 1978, Kay and Nedderman, 1985, Tritton, 1988) and 0.04 (Targ, 1951, Lew and Fung, 1970). The last value is equal to the inlet length in a straight channel with flat parallel walls (Schlichting, 1955, Brodkey, 1995). In order to take into account the between-author variability of the dimensionless entry length, a range is sometimes provided ($Le/(d_h.Re) \in [0.03 - 0.06]$, $100 < Re < 2000$ (Joulié, 1998).

[5] The Reynolds number threshold of 200 is author-dependant, a value of 100 is often given.

[6] $Le = 0.061Re + 0.72/(0.04Re + 1)$ (Liepsch, 1986).

[7] $Le/d_h = 0.59 + 0.056Re$ (Atkinson *et al.*, 1969).

[8] $Le/d_h = 0.056Re + 0.6/(0.035Re + 1)$ (Shah and London, 1978).

Barbee, K.A.; Davies, P.F.; Ratneshwar, L. (1994): Shear stress-induced reorganization of the surface topography of living endothelial cells imaged by atomic force microscopy. *Circ. Res.*, vol. 74, pp. 163-171.

Bassez, S.; Flaud, P.; Chauveau, M. (2001): Modeling of the deformation of flexible tubes using a single law: application to veins of the lower limb in man. *ASME J. Biomech. Eng.*, vol. 123, pp. 58-65.

Bonis, M.; Ribreau, C.; Verchery, G. (1981): Etude théorique et expérimentale de l'aplatissement d'un tube élastique en dépression. *J. Méca. Appl.*, vol. 5, pp. 123-144.

Boukir, K.; Maday, Y.; Metivet, B. (1992): A high order characteristics method for incompressible Navier-Stokes equations. *Proceedings of International Conference on Spectral and High Order Method*, Montpellier, France, June 1992.

Boussinesq, J. (1891): Calcul de la moindre longueur que doit avoir un tube circulaire, évasé à son entrée, pour qu'un régime sensiblement uniforme s'y établisse. *Comptes Rendus Acad. Sci. (Paris)*, vol. 113, pp. 49-51.

Brodkey, R.S. (1995): *The Phenomena of Fluid Motion*, Dover, New York.

Caro, C.G.C.; Pedley, T.J.; Schroter, R.C.; Seed, W.A. (1978): *The Mechanics of the Circulation*, Oxford University Press, Oxford.

Chien, S. (1970): Shear dependence of effective cell volume as a determinant of blood viscosity. *Science*, vol. 168, pp. 977-978.

Chien, S. (1975): Biophysical behavior in suspensions, in *The Red Blood Cell*, D. Surgenor (ed.) Academic Press, New York.

Comolet, R. (1976): *Mécanique Expérimentale des Fluides*, Tome II, Masson, Paris.

Cottet, G.-H.; Koumoutsakos, P. (2000): *Vortex methods: theory and practice*, Cambridge University Press, Cambridge.

DePaola, N.; Dewey, C.F.; Davies, P.F.; and Gimbrone, M.A. (1992): Vascular endothelium responds to fluid shear stress gradients. *Arterioscler. Thromb. Vasc. Biol.*, vol. 12, pp. 1254-1259.

Fediaevski, C.; Voitkounski, I.; Faddeev, Y. (1974): *Mécanique des Fluides*, Mir, Moscou.

Franke, R.-P.; Gräfe, M.; Schnittler, H.; Seiffge, D.; Mittermayer, D.; Drenckhahn, D. (1984): Induction of human vascular endothelial stress fibers by fluid shear stress. *Nature*, vol. 307, pp. 648-649.

Glowinski, R. (1984): *Numerical methods for nonlinear variational problems*, Springer Series in Computational Physics, Springer-Verlag, New York.

Goldstein, S. (1938): *Modern Developments in Fluid Dynamics*, Tome I, Oxford University Press, London.

Haond, C.; Ribreau, C.; Boutherin-Falson, O.; Finet, M. (1999): Laminar flow through a model of collapsed veins. Morphometric response of endothelial vascular cells to a longitudinal shear stress non uniform crosswise. *Europ. Phys. J. AP*, vol. 8, pp. 87-96.

Janna, W.S. (1998): Internal Incompressible Viscous Flow. In R.W. Johnson (ed) *Handbook of Fluid Dynamics*, CRC Press, Boca Raton, pp. 5-63.

Joulié, R. (1998) *Mécanique des Fluides Appliquée*, Ellipses, Paris.

Kay, J.M.; Nedderman, R.M. (1985): *Fluid Mechanics and Transfer Processes*, Cambridge University Press, Cambridge, UK.

Langhaar, H.L. (1942): Steady flow in the transition length of a straight tube. *Trans. ASME J. Appl. Mechanics*, vol. 64, pp. A55.

Laurent, V.; Planus, E.; Isabey, D.; Lacombe, C.; Bucherer, C.; (2000) Propriétés mécaniques de cellules endothéliales évaluées par micromanipulation cellulaire et magnétocytométrie. In: C. Ribreau *et al.* (eds) *MécanoTransduction 2000*, Tec&Doc, Paris, pp. 373-380.

Lenormand, G.; Hénon, S.; Gallet, F.; (2000) Détermination des modules élastiques du cytosquelette du globul rouge humain par pinces optiques. In: C. Ribreau *et al.* (eds) *MécanoTransduction 2000*, Tec&Doc, Paris, pp. 389-394.

Lew, H.S.; Fung, Y.C. (1970): Entry flow into blood vessels at arbitrary Reynolds number. *J. Biomechanics*, vol. 3, pp. 23-38.

Liepsch, D. (1986): Flow in tubes and arteries. *Biorheology*, vol. 23, pp. 395-433.

Mc Donald, D.A. (1974): *Blood Flow in Arteries*, Edward Arnold, London.

Naili, S.; Ribreau, C. (1999): Wall shear stress in collapsed tubes. *Europ. Phys. J. AP*, vol. 5, pp. 95-100.

Olesen, S.P.; Clapham, D.E.; Davies, P.F. (1988): Haemodynamic shear stress activates a K^+ current in vascular endothelial cells. *Nature*, vol. 331, pp. 168-170.

Padet, J. (1991): *Fluides en Ecoulement*, Masson, Paris.

Pironneau, O. (1982): On the transport-diffusion algorithm and its application to the Navier-Stokes Equations. *Numerische Mathematik*, vol. 38, pp. 309-332.

Ribreau, C.; Naili, S.; Bonis, M.; Langlet, A. (1993): Collapse of thin-walled elliptical tubes for high values of major-to-minor axis ratio. *ASME J. Biomech. Eng.*, vol. 115, pp. 432-440.

Ribreau, C.; Naili, S.; Langlet, A. (1994): Head losses in smooth pipes obtained from collapsed tubes. *J. Fluids Structures*, vol. 8, pp. 183-200.

Ribreau, C.; Thiriet, M. (1998): Ecoulements veineux. In: M. Jaffrin, F. Goubel (eds) *Biomécanique des fluides et des tissus*, Masson, Paris, pp. 131-178.

Schiller, L. (1922): Die Entwicklung der laminaren Geschwindigkeitsverteilung und ihre Bedeutung für Zähigkeitsmessungen. *Z. angew. Math. Mech.*, vol. 2, pp. 96-106.

Schlichting, H. (1955): *Boundary-Layer Theory*, McGraw Hill, New York.

Shah, R.K.; London, A.L. (1978): *Laminar Flow Forced Convection in Ducts*, Academic Press, New York.

Shames, I.H. (1992): *Mechanics of Fluid*, McGraw Hill, New York.

Sparrow, E.M.; Lin, S.H.; Lundgren, T.S. (1964): Flow development in the hydrodynamic entrance region of tubes and ducts. *Phys. Fluids*, vol. 7, pp. 338-347.

Sun, R.J.; Muller, S.; Wang, X.; Lucius, M.; Stolz, J.F. (2000): Effect of shear stress on the regulation of von Willebrand factor of human endothelial cells. In: C. Ribreau *et al.* (eds) *MécanoTransduction 2000*, Tec&Doc, Paris, pp. 341-348.

Targ, S.M. (1951): Basic problems of the theory of laminar flows. (Russian publication), Moskva.

Thiriet, M.; Naili, S.; Langlet, A.; Ribreau, C. (2001): Flow in thin-walled collapsible tubes. In: C. Leondes (ed) *Biofluid methods in vascular and pulmonary systems*, CRC Press, Boca Raton, chap. 10, pp. 1-43.

Tritton, D.J. (1988): *Physical Fluid Dynamics*, Oxford University Press, Oxford.